2021 43rd Annual International Conference of the
IEEE Engineering in Medicine & Biology Society (EMBC)
Oct 31 - Nov 4, 2021. Virtual Conference

Extended Blind End-member and Abundance Estimation with Spatial Total Variation for Hyperspectral Imaging

Inés A. Cruz-Guerrero[1], Daniel U. Campos-Delgado[1],*Senior Member, IEEE*, and Aldo R. Mejía-Rodríguez[1]

***Abstract*— Blind linear unmixing (BLU) methods allow the separation of multi and hyperspectral data into end-members and abundance maps in an unsupervised fashion. However, due to incident noise, the abundance maps can exhibit high presence of granularity. To address this problem, in this paper, we present a novel proposal for BLU that considers spatial coherence in the abundance estimations, through a total spatial variation component. The proposed BLU formulation is based on the blind end-member and abundance extraction perspective with total spatial variation (EBEAE-STV). In EBEAE-STV, internal abundances are added to incorporate the spatial coherence in the cost function, which is solved by a coordinates descent algorithm. The results with synthetic data show that the proposed algorithm can significantly decrease the granularity in the estimated abundances, and the estimation errors and computational times are lower compared to state of the art methodologies.**

***Clinical relevance*— The proper and robust estimation of end-members and their respective contributions (abundances) in multi-spectral and hyper-spectral images from the proposed EBEAE-STV methodology might provide useful information in several biomedical applications, such as chemometric analysis on different biological samples, tumor identification and brain tissue classification for hyper-spectral imaging, among others.**

I. Introduction

Hyperspectral imaging is a powerful tool for acquiring information remotely, with multiple applications in the biomedical engineering field, for example to classify biological tissue and to identify dermatological diseases [1]–[4]. A hyperspectral image (HSI) can be visualized as a three-dimensional dataset, where each pixel in the 2D spatial domain has a spectral response with hundreds or thousands of bands that provide detailed information of the region or sample analyzed [5], [6]. In a HSI, a pure component in a given pixel is denoted as spectral signature or end-member, while its contributions per pixel are called abundances [6]. Nonetheless, most of the times, the information captured by a HSI corresponds to the spectral mixture of different pure materials due to a low spatial resolution, and multiple dispersion during acquisition, which makes the analysis of these images a challenging task [6]. To overcome this problem, a processing stage has to take advantage of the information present in the HSI by identifying properties and characteristics of each element in an independent way; these processing techniques are known as hyperspectral unmixing (HU) [7].

HU methods are a set of mathematical tools to obtain the corresponding abundance maps of a HSI from given end-members (supervised perspective) [5], but if both end-members and abundance maps are estimated jointly in a unsupervised way, then this problem is called blind hyperspectral unmixing [6], [8]. The most widely used HU methods in the literature are based on a linear mixture model (LMM) for each pixel, due to their relative simplicity and practicality [9]–[11]. Thus, the joint estimation of end-members and their abundances in a HSI by a LMM is denoted as blind linear unmixing (BLU); a recent example of BLU is the extended blind end-member and abundance extraction (EBEAE) methodology [8]. Although LMM have proven to be efficient in estimating end-members and abundances from HSI, the resulting methods are susceptible to the presence of noise from various sources and light scattering from adjacent pixels [12]. In addition, all LMM techniques perform an analysis in discrete locations, so that they can produce granularity in the abundance maps, generating unwanted estimation errors [12], [13].

In recent years, proposals have emerged that attempt to compensate for the shortcomings of LMMs, such as performing a filtering stage prior to the unmixing stage and, more recently, adding spatial coherence information to the HU process, reducing the impact of noise and the estimation in discrete locations [14], [15]. Nevertheless, by considering the neighboring pixel information in the HU methods, the computational complexity and control variables are increased, which produces large execution times [16].

In this context, we present a new version of EBEAE, which considers in its formulation spatial coherence information by means of the total variation theory, called EBEAE with spatial total variation (EBEAE-STV). In order to generate a controlled environment for the validation process, the EBEAE-STV algorithm is evaluated with synthetic datasets from near-infrared (VNIR) images by adding various types and levels of noise. Also, EBEAE-STV is compared with three methodologies in the state of the art, which illustrates the improved performance of the proposal.

II. Problem Formulation

In our formulation, we assume the existence of K measurements of a physical variable, expressed as real-valued L-dimensional vectors $\mathbf{z}_k \in \mathbb{R}^L$ with $k \in [1, K]$. In addition,

This work was supported by the CONACYT through a Basic Science grant No. 254637. The work of Inés A. Cruz-Guerrero was supported by CONACYT through a doctoral grant (# 865747).

[1] Inés A. Cruz-Guerrero, Daniel U. Campos-Delgado and Aldo R. Mejía-Rodríguez are with Facultad de Ciencias, and Daniel U. Campos-Delgado also with Instituto de Investigación en Comunicación Óptica, both in Universidad Autónoma de San Luis Potosí, S.L.P., México (e-mails: a211439@alumnos.uaslp.mx, ducd@fciencias.uaslp.mx, aldo.mejia@uaslp.mx).

the set of measurements $\mathcal{Z} = \{\mathbf{z}_1, \ldots, \mathbf{z}_K\}$ is normalized, so that each element is scaled to add up to one, such that $\mathbf{y}_k = \frac{1}{\mathbf{1}_L^T \mathbf{z}_k}\mathbf{z}_k \ \forall k$. For the scaled set of measurements $\mathcal{Y} = \{\mathbf{y}_1, \ldots, \mathbf{y}_K\}$, we assume that the k-th element can be represented by a linear mixture model of N-th order:

$$\mathbf{y}_k = \sum_{n=1}^{N} \alpha_{k,n}\mathbf{p}_n + \mathbf{v}_k = \underbrace{[\mathbf{p}_1, \ldots, \mathbf{p}_N]}_{\mathbf{P}\in\mathbb{R}^{L\times N}} \underbrace{\begin{bmatrix}\alpha_{k,1}\\ \vdots \\ \alpha_{k,N}\end{bmatrix}}_{\boldsymbol{\alpha}_k\in\mathbb{R}^N} + \mathbf{v}_k, \quad (1)$$

where $\mathbf{p}_n \in \mathbb{R}^L$ is the n-th end-member $\forall n \in [1, N]$ ($\mathbf{p}_n \geq 0$ and $\mathbf{1}_L^\top \mathbf{p}_n = 1$), while $\alpha_{k,n} \geq 0$ represents its abundance in the k-th measurement. The abundances in k-th spatial location are normalized, i.e. $\mathbf{1}_N^\top \boldsymbol{\alpha}_k = 1$. The vector $\mathbf{v}_k$ represents independently and identically distributed Gaussian noise, with zero mean and finite covariance matrix. The scaled measurements, abundances and noise vectors can be represented in matrix notation as $\mathbf{Y} = [\mathbf{y}_1 \cdots \mathbf{y}_K] \in \mathbb{R}^{L\times K}$, $\mathbf{A} = [\boldsymbol{\alpha}_1 \ldots \boldsymbol{\alpha}_K] \in \mathbb{R}^{N\times K}$, and $\mathbf{V} = [\mathbf{v}_1 \ldots \mathbf{v}_K] \in \mathbb{R}^{L\times K}$, respectively; so the LMM is expressed as $\mathbf{Y} = \mathbf{PA} + \mathbf{V}$.

The estimation problem departs from the EBEAE methodology in [8] by proposing a modification of the energy functional to take into account spatial coherence. This new synthesis problem can be described as

$$\min_{\mathbf{A},\mathbf{P},\mathbf{W}} \frac{1}{2K}\sum_{k=1}^{K}\frac{\|\mathbf{y}_k - \mathbf{P}\boldsymbol{\alpha}_k\|^2}{\|\mathbf{y}_k\|^2} + \frac{\rho}{2\vartheta}\sum_{n=1}^{N-1}\sum_{j=n+1}^{N}\|\mathbf{p}_n - \mathbf{p}_j\|^2 + \frac{\lambda}{2K}\sum_{k=1}^{K}\|\mathbf{w_k} - \boldsymbol{\alpha_k}\|^2 + \frac{\tau}{K}HTV(\mathbf{W}), \quad (2)$$

with ρ, λ, τ as regularization weights, and $\vartheta \triangleq 1 + \ldots + (N-1)$ for all $N \geq 2$. On the other hand, we introduce new internal abundance vectors $\{\mathbf{w}_k\}_{k=1}^K$, which are gathered in $\mathbf{W} = [\mathbf{w}_1, ..., \mathbf{w}_K] \in \mathbb{R}^{N\times K}$ that corresponds to the matrix of internal abundances. The functional $HTV(.)$ is a hyperspectral total variation regularization term that considers a spatial correlation, as proposed in [15]. In this way, the optimization in (2) can be solved with three decoupled subproblems by a coordinates descent scheme [17]: End-members estimation $\mathbf{P}$, abundances computation $\mathbf{A}$, and internal abundance extraction $\mathbf{W}$. To obtain the solution of these sub-problems, a restricted quadratic optimization approach with coordinates descent scheme is followed, that is, the matrices of two sub-problems are kept fixed, while the remaining one is optimized until convergence of the overall estimation error or the maximum number of iterations is reached [8], [17]. Consequently, in this proposal, the estimation of the internal abundances in $\mathbf{W}$ is added to the EBEAE problem, so the energy functional in (2) is updated. Meanwhile, the end-members estimation follows the original formulation in [8].

A. End-members Estimation

In this sub-problem, we assume that the abundances matrices $\mathbf{A}$ and $\mathbf{W}$ remain fixed in the estimation process, and by rewriting (2), we obtain

$$\min_{\mathbf{P}\geq 0} \frac{1}{2K}\sum_{k=1}^{K}\frac{\|\mathbf{y}_k - \mathbf{P}\boldsymbol{\alpha_k}\|^2}{\|\mathbf{y}_k\|^2} + \frac{\rho}{2\vartheta}\sum_{n=1}^{N-1}\sum_{j=n+1}^{N}\|\mathbf{p}_n - \mathbf{p}_j\|^2, \quad (3)$$

with the restriction $\mathbf{P}^\top \mathbf{1_L} = \mathbf{1_N}$. To meet the constraints of the previous problem, a Lagrange multiplier is added for the equality condition in the cost function, and the stationary conditions for the optimal value are derived to obtain a closed-solution. In this synthesis problem, the parameter ρ plays an important role in (3), since when $\rho \approx 1$ the resulting end-members will exhibit similar morphological characteristics; meanwhile when $\rho \approx 0$ the end-members can be very different.

B. Abundances Estimation

The second sub-problem is solved for each measurement in $\mathcal{Y}$, and assumes that the matrices $\mathbf{W}$ and $\mathbf{P}$ are known a priori. Hence, the abundances estimation $\boldsymbol{\alpha}_k$ for k-th measurement is formulated from (2) as

$$\min_{\boldsymbol{\alpha_k}\geq 0} \frac{1}{2}\|\mathbf{y}_k - \mathbf{P}\boldsymbol{\alpha}_k\|^2 + \frac{\lambda\hat{y}_k}{2}\|\mathbf{w}_k - \boldsymbol{\alpha}_k\|^2, \quad (4)$$

with $\boldsymbol{\alpha}_k^\top \mathbf{1}_N = 1$ and by defining the constant $\hat{y}_k = \|\mathbf{y}_k\|^2$. As in the case of the previous sub-problem, a Lagrange multiplier is included in (4) to ensure the equality restriction, and a closed-form solution can be deduced, as described in [8].

C. Internal Abundances Estimation

In the next step, the abundance matrix $\mathbf{A}$ is known and remains fixed to estimate the internal abundances matrix $\mathbf{W}$. For this estimation, a vector representation is used in (2) and solve it per each end-member index n:

$$\min_{\mathbf{W}_n} \frac{\lambda}{2K}\|\mathbf{W}_n - \mathbf{A}_n\|^2 + \frac{\tau}{K}\|\mathbf{W}_n\mathbf{D}_x^\top\|_1 + \frac{\tau}{K}\|\mathbf{W}_n\mathbf{D}_y^\top\|_1, \quad (5)$$

where $\mathbf{A}_n \in \mathbb{R}^{1\times K}$ and $\mathbf{W}_n \in \mathbb{R}^{1\times K}$ denote the n-th row in $\mathbf{A}$ and $\mathbf{W}$, respectively, i.e. these row vectors represent the nominal and internal abundances of n-th end-member; $\mathbf{D}_x \in \mathbb{R}^{K\times K}$ and $\mathbf{D}_y \in \mathbb{R}^{K\times K}$ represent horizontal and vertical 2-D finite difference operators applied to the internal abundances, with a zero adjustment at the borders to maintain the original dimensions [15]. In (5), $\|\cdot\|$ denotes the Euclidean norm, and $\|\cdot\|_1$ the 1-norm for vectors.

The optimization problem (5) is high-dimensional, non-differentiable by the 1-norm, and $\mathbf{W}_n$ is not separable. To solve this problem, we first introduce new variables $\mathbf{R} = \mathbf{W}_n\mathbf{D}_x^\top$ and $\mathbf{Q} = \mathbf{W}_n\mathbf{D}_y^\top$ in (5) to reformulate the optimization problem as suggested in [15]:

$$\min_{\mathbf{W}_n,\mathbf{R},\mathbf{Q}} \frac{\lambda}{2}\|\mathbf{W}_n - \mathbf{A}_n\|^2 + \tau\|\mathbf{R}\|_1 + \tau\|\mathbf{Q}\|_1 + \frac{\nu}{2}\|\mathbf{R} - \mathbf{W}_n\mathbf{D}_x^\top\|^2 + \frac{\nu}{2}\|\mathbf{Q} - \mathbf{W}_n\mathbf{D}_y^\top\|^2, \quad (6)$$

where ν is a regularization parameter for both horizontal and vertical terms to consider equal contributions.

Finally, the expression in (6) can be divided into three subproblems by means of the Bregman division, which are relatively easy to solve as shown in [15] and [18]. Once obtained the internal abundances $\mathbf{W}$, when solving (5), a process of linear rectification is applied to guarantee positivity in each element, and each column in $\mathbf{W}$ is normalized to add one.

III. Experimental Results and Discussion

In this section, we demonstrate the application of the proposed algorithm in synthetic VNIR images [8]. To compare the performance of the proposed algorithm, we implemented three popular linear decomposition algorithms which consider spatial coherence information in their formulation: graph-regularized $L_{1/2}$ nonnegative matrix factorization (GLNMF) [19], preserving the intrinsic structure invariant nonnegative matrix factorization (PISINMF) [7], and nonnegative matrix factorization-quadratic minimum volume (NMF-QMV) [20]. All the algorithms were implemented numerically in Matlab 2018a, and on a computer with an Intel Core i7 quad-core processor with 16 GB of RAM. In addition, the threshold of convergence of the methods was generally set at $\epsilon = 0.001$, with a maximum number of iterations of 20.

To test the effectiveness of the proposed method in challenging conditions, two types of noise commonly present in HSIs were added to the synthetic images: Gaussian noise and shot noise. In order to produce a measurement $\mathbf{y}_k$ with both types of noise, from a noise-less measurement $\mathbf{y}_k^0$, the following mapping is applied:

$$\mathbf{y}_k = \mathbf{y}_k^0 + \mathbf{n}_k + \mathbf{m}_k \cdot \sqrt{\mathbf{y}_k^0} \qquad \forall k \in [1, K], \tag{7}$$

where $\mathbf{n}_k \in \mathbb{R}^L$ and $\mathbf{m}_k \in \mathbb{R}^L$ are vectors associated with the noise components. In our approach, the Gaussian noise vector $\mathbf{n}_k$ has zero mean and standard deviation σ_k^{SNR}. On the other hand, the noise component $\mathbf{m}_k$ is related to the induced shot noise, and is also defined by a Gaussian distribution with zero mean and standard deviation σ_k^{PSNR}. In our formulation, σ_k^{SNR} and σ_k^{PSNR} are defined by the desired signal to noise ratio (SNR), and peak signal to noise ratio ($PSNR$):

$$\sigma_k^{SNR} = \sqrt{\frac{\|\mathbf{y}_k^0\|^2}{10^{\frac{SNR}{10}}}}, \quad \sigma_k^{PSNR} = \sqrt{\frac{\max_{l\in[1,L]}(\mathbf{y}_k^0)_l^2}{10^{\frac{PSNR}{10}}}}. \tag{8}$$

The studied noise levels were $(SNR, PSNR) \in \{(20,10),(25,15),(30,20),(35,25),(40,30),(45,35),(50,40)\}$ dB, which are challenging values for any HU method. In addition, for each combination of SNR and PSNR, a Monte Carlo evaluation was carried out over 50 noise realizations, thus generating a meaningful statistic. Also, to quantify the precision in the BLU process, the sets of estimated end-members and abundances were defined as $\mathcal{A}$ and $\mathcal{P}$, respectively, and their counterparts in the synthetic data $\bar{\mathcal{A}}$ and $\bar{\mathcal{P}}$, and then the approximation errors were calculated as [21]:

$$E_p = \frac{1}{card(\overline{\mathcal{P}}) + card(\mathcal{P})} \min_{\forall \overline{\mathbf{p}}\in\overline{\mathcal{P}}, \mathbf{p}\in\mathcal{P}} \|\overline{\mathbf{p}} - \mathbf{p}\|, \tag{9}$$

$$E_a = \frac{1}{card(\overline{\mathcal{A}}) + card(\mathcal{A})} \min_{\forall \hat{\boldsymbol{\alpha}}\in\overline{\mathcal{A}}, \boldsymbol{\alpha}\in\mathcal{A}} \|\hat{\boldsymbol{\alpha}} - \boldsymbol{\alpha}\|. \tag{10}$$

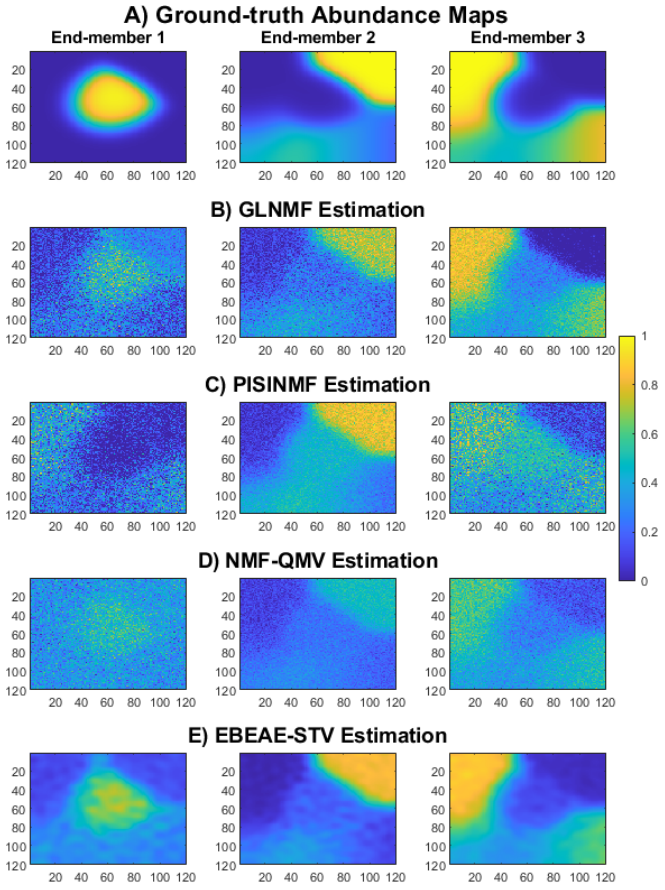

Fig. 1. One realization of the Monte Carlo estimation results (abundance maps) for VNIR synthetic datasets ($N = 3$, $SNR = 35$ dB and $PSNR = 25$ dB): A) Ground-truth, B) GLNMF, C) PISINMF, D) NMF-QMV, and E) EBEAE-STV.

The synthetic VNIR hyperspectral image was generated with three components ($N = 3$) over a spatial domain of 120×120 pixels (see top row in Fig. 1), with a pixel spectral response in the range of 450 nm to 950 nm and 129 bands, as described in [8]. An exhaustive search of the hyperparameters of the methods GLNMF, PISINMF, and NMF-QMV was carried out by choosing the values that generated the least amount of abundance error. The estimation results for one realization in the Monte Carlo evaluation with large noise ($SNR = 35$ dB, $PSNR = 25$ dB) are shown in the Fig. 1, where it can be seen that in general all the HU methods produce an error in the estimated regions, however, the results produced by EBEAE-STV correspond to a greater extent with the ground-truth, and with a significant decrease in the granularity, which is still visible in the comparison methods.

Finally, the mean results of abundances errors in (10) and end-members errors in (9) of the Monte Carlo test

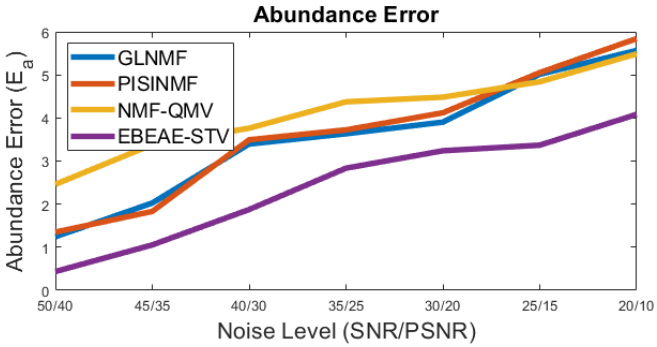

(a) Abundance Error

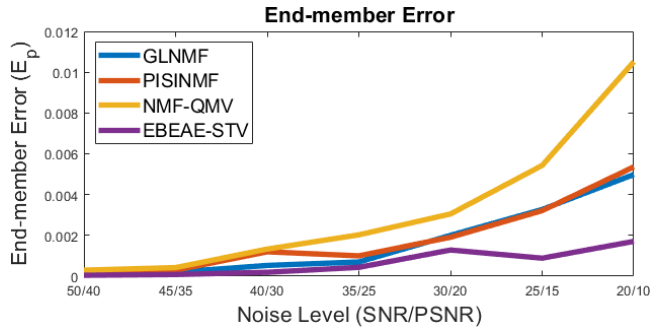

(b) End-member Error

Fig. 2. Monte Carlo evaluation for abundances and end-members estimation errors in VNIR synthetic datasets ($N = 3$) under different SNR and $PSNR$ values: Comparison EBEAE-STV with state of the art HU algorithms.

are presented in the Fig. 2. For all methods, as the noise level $(SNR, PSNR)$ increased, the errors (E_p, E_a) also raised. In both plots, EBEAE-STV clearly exhibits the lowest error, and the second lower performance is achieved by PISINMF and NMF-QMV. On the other hand, the average computational times (mean $\pm$ standard deviation) for each method were 127.82 ± 3.35 s for GLNMF, 13.74 ± 0.38 s for NMF-QMV, 5.56 ± 0.17 s for PISINMF, and 2.40 ± 0.16 s for EBEAE-STV. Consequently, EBEAE-STV was 56% faster than the algorithm with the shortest execution time among the proposals in the state of the art. Hence, EBEAE-STV improved the comparison methodologies in terms of estimation accuracy and computational time.

IV. Conclusion

In this work, we presented a new version of the EBEAE algorithm, which considers spatial coherence by total variation techniques for the blind estimation of end-members and abundances in hyperspectral images. Our experiments showed that the EBEAE-STV method improves abundance map estimates by largely eliminating the granularity caused by noise in the measurements, and the effect of discrete locations. Our synthetic evaluation showed that EBEAE-STV obtains the best estimation performance with the lowest computational time with respect to previous efforts in the literature. In a future work, we will expand our evaluation with other types of multi-spectral images used in the biomedical engineering field, and will consider the evaluation of experimental datasets.

References

[1] A. Hosking et al., "Hyperspectral imaging in automated digital dermoscopy screening for melanoma," *Lasers in Surgery and Medicine*, vol. 51, no. 3, pp. 214–222, 2019.

[2] H. Fabelo et al., "Dermatologic hyperspectral imaging system for skin cancer diagnosis assistance," in *2019 XXXIV Conference on Design of Circuits and Integrated Systems (DCIS)*, pp. 1–6, 2019.

[3] E. Baltussen et al., "Hyperspectral imaging for tissue classification, a way toward smart laparoscopic colorectal surgery," *Journal of Biomedical Optics*, vol. 24, no. 1, pp. 1 – 9, 2019.

[4] B. Fei et al., "Label-free hyperspectral imaging and quantification methods for surgical margin assessment of tissue specimens of cancer patients," in *39th Annual International Conference of the IEEE Engineering in Medicine and Biology Society (EMBC)*, pp. 4041–4045, 2017.

[5] F. Xiong, Y. Qian, J. Zhou, and Y. Y. Tang, "Hyperspectral Unmixing via Total Variation Regularized Nonnegative Tensor Factorization," *IEEE Trans. Geosci. Remote Sens.*, vol. 57, no. 4, pp. 2341–2357, 2019.

[6] J. Qin et al., "Blind Hyperspectral Unmixing Based on Graph Total Variation Regularization," *IEEE Trans. Geosci. Remote Sens.*, pp. 1–14, Early Access, 2020.

[7] Y. Shao, J. Lan, Y. Zhang, and J. Zou, "Spectral unmixing of hyperspectral remote sensing imagery via preserving the intrinsic structure invariant," *Sensors (Switzerland)*, vol. 18, no. 10, 2018.

[8] D. U. Campos-Delgado, O. Gutierrez-Navarro, J. J. Rico-Jimenez, E. Duran-Sierra, H. Fabelo, S. Ortega, G. Callico, and J. A. Jo, "Extended Blind End-Member and Abundance Extraction for Biomedical Imaging Applications," *IEEE Access*, vol. 7, pp. 178539–178552, 2019.

[9] T. Imbiriba, R. A. Borsoi, and J. C. M. Bermudez, "Low-rank tensor modeling for hyperspectral unmixing accounting for spectral variability," *IEEE Transactions on Geoscience and Remote Sensing*, vol. 58, no. 3, pp. 1833–1842, 2018.

[10] J. Yao, D. Meng, Q. Zhao, W. Cao, and Z. Xu, "Nonconvex-sparsity and nonlocal-smoothness-based blind hyperspectral unmixing," *IEEE Transactions on Image Processing*, vol. 28, no. 6, pp. 2991–3006, 2019.

[11] N. Dobigeon, J.-Y. Tourneret, C. Richard, J. C. M. Bermudez, S. McLaughlin, and A. O. Hero, "Nonlinear unmixing of hyperspectral images: Models and algorithms," *IEEE Signal Process. Mag.*, vol. 31, no. 1, pp. 82–94, 2013.

[12] J. M. P. Nascimento and J. M. Bioucas-Dias, "Nonlinear mixture model for hyperspectral unmixing," *Image Signal Process. Remote Sens. XV*, vol. 7477, no. September 2009, p. 74770I, 2009.

[13] W. He, H. Zhang, and L. Zhang, "Total variation regularized reweighted sparse nonnegative matrix factorization for hyperspectral unmixing," *IEEE Trans. Geosci. Remote Sens.*, vol. 55, no. 7, pp. 3909–3921, 2017.

[14] Y. Q. Zhao and J. Yang, "Hyperspectral image denoising via sparse representation and low-rank constraint," *IEEE Trans. Geosci. Remote Sens.*, vol. 53, no. 1, pp. 296–308, 2015.

[15] H. K. Aggarwal and A. Majumdar, "Hyperspectral Image Denoising Using Spatio-Spectral Total Variation," *IEEE Geosci. Remote Sens. Lett.*, vol. 13, no. 3, pp. 442–446, 2016.

[16] H. Li, R. Feng, L. Wang, Y. Zhong, and L. Zhang, "Superpixel-Based Reweighted Low-Rank and Total Variation Sparse Unmixing for Hyperspectral Remote Sensing Imagery," *IEEE Trans. Geosci. Remote Sens.*, vol. 59, no. 1, pp. 629–647, 2021.

[17] D. G. Luenberger and Y. Ye, *Linear and Nonlinear Programming*. Springer-verlag, 4th ed., 2016.

[18] X. Liu and L. Huang, "Split Bregman iteration algorithm for total bounded variation regularization based image deblurring," *J. Math. Anal. Appl.*, vol. 372, no. 2, pp. 486–495, 2010.

[19] X. Lu, H. Wu, Y. Yuan, P. Yan, and X. Li, "Manifold regularized sparse NMF for hyperspectral unmixing," *IEEE Trans. Geosci. Remote Sens.*, vol. 51, no. 5, pp. 2815–2826, 2013.

[20] L. Zhuang, C. H. Lin, M. A. Figueiredo, and J. M. Bioucas-Dias, "Regularization parameter selection in minimum volume hyperspectral unmixing," *IEEE Trans. Geosci. Remote Sens.*, vol. 57, no. 12, pp. 9858–9877, 2019.

[21] A. Conci and C. Kubrusly, "Distances between sets — A survey," *arXiv*, vol. 26, pp. 1–14, 2018.